To cite this article: S. Magalhães, J. S. Cabaço, R. Mateus, D. Nd. Faye, D. R. Pereira, M. Peres, K. Lorenz, C. Díaz-Guerra, J. P. Araújo , E. Alves, ***CrystEngComm***, 2021,**23**, 2048-2062

DOI: 10.1039/D0CE01669A

Crystal mosaicity determined by a novel layer de-convolution Williamson-Hall method

S. Magalhães[a], J. S. Cabaço[b], R. Mateus[a], D. Nd. Faye[a,c], D. R. Pereira[a,c], M. Peres[a,c], K. Lorenz[a,c], C. Díaz-Guerra[d], J. P. Araújo[b] , E. Alves[a]

[a]*IPFN, Instituto de Plasmas e Fusão Nuclear, Campus Tecnológico e Nuclear, Instituto Superior Técnico, Universidade de Lisboa, Estrada Nacional 10, 2695-066 Bobadela LRS, Portugal.*

[b]*IFIMUP/IN, Instituto de Física dos Materiais da Faculdade de Ciências da Universidade do Porto, Instituto de Nanociência e Nanotecnologia, Rua do Campo Alegre, 687 4169-007 Porto, Portugal.*

[c]*Instituto de Engenharia de Sistemas de Computadores-Microsystems and Nanotechnology (INESC-MN), Lisboa, Portugal*

[d]*Departamento de Física de Materiales, Facultad de Ciencias Físicas, Universidad Complutense de Madrid, Ciudad Universitaria s/n, 28040,Madrid, Spain*

Abstract The application of conventional Williamson-Hall plot (WH) analysis to crystals often results in broadenings not proportional to the scattering length vector. Several reasons may influence the broadening such as composition or strain heterogeneities, wafer curvature, dislocation anisotropy and other defects. In this work, linearization of WH plots is achieved given the assumption that the total crystal size may be de-convoluted into a finite number of layers, each with constant thickness, strain and mosaic spread. The novel linearization algorithm, LdCWH, acronym for layer de-convolution WH method, employs a finite number of Pseudo-Voigts (PVs) functions for each measurement. Afterwards, it searches for possible solutions by changing the PVs coefficients until r^2 of the conventional WH representation is above 0.999. The searching procedure consists in a combination of a Genetic algorithm (GA) to generate randomly the PV coefficients within a specified range and a Marquardt-Levenberg algorithm to fit simultaneously the measured reflections using the PV coefficients as inputs. The possible solutions further allow estimating the upper and lower bounds of the mosaicity. Conventional WH plots and the implementation of the LdCWH are applied and discussed on a commercial AlGaN thick layer and to bulk α-MoO_3 crystals. For the former, (lateral and perpendicular) coherence lengths, tilt angle and heterogeneous strain derived are 616±7 nm, 510±10 nm, 0.069±0.001º and 0.0345±0.0002%, respectively, while for the latter, vertical coherence length of 3883±56 nm and heterogeneous strain of 0.0556±0.0002% is found. The nature of peak broadening as for integral breadth and full width at half maximum is discussed.

Keywords: Williamson-Hall; Mosaicity; X-ray diffraction; Defects

Corresponding author: smagalhaes@ctn.tecnico.ulisboa.pt

1. Introduction

Williamson-Hall (WH) as well as size-strain plots are very useful techniques to describe the mosaicity (coherence lengths being parallel or perpendicular to the substrate surface, tilt angles and heterogeneous strains) of a crystal.[1-10] The WH method consists in the separation of size and strain effects given the assumption that the broadening in the reciprocal space due to coherence length is scattering vector length independent and broadening in the reciprocal space due to tilt angle or strain is scattering order dependent. Assuming that broadenings due to instrumentation, wafer bending, dislocation anisotropy and impurities plays no significant role in the total broadening, a graphical method to evaluate crystalline mosaicity is, then, applicable. The linear fit coefficients correlate directly to the physical quantities described by the mosaicity. Extensions or so-called modified WH (m-WH) were also developed for the particular case of strain broadening caused by dislocations.[11-13] In the m-WH plots the linearization is achieved by asserting dislocations to give different contrasts depending on the relative positions of the Burgers and line vectors of the dislocations and the diffraction vector. On the other hand, other methods such as Fourier analysis of the diffraction peaks[14-17] and analytical empirical methods using Pseudo-Voigts functions are currently employed to estimate the crystalline mosaicity.[14,18,19] Fourier analysis consists in a special logarithmic series expansion of the Fourier coefficients of Bragg reflection peak profiles, whereas the analytical method foundations are focused on the Pseudo-Voigt broadening. The latter envelops a linear combination of a Gaussian and Lorentzian functions to simulate the rocking curve or the 2θ-ω scans. Thus, peak width and shape are accessed through mathematical fitting of the measured curve. A dominant peak broadening driven by high tilts is described by a Gaussian-like profile, while low coherence lengths settle into a more pronounced Lorentzian shape profile. All the above methods assume homogeneous distribution of the mosaicity which often is not the most realistic case. In particular, in III-nitrides grown on sapphire, one of the most common substrates, the lattice mismatch between both crystals leads to high biaxial strain which is relaxed as the film thickness increases. As an example, gallium nitride grown on c - sapphire substrate is compressively strained due to a lattice mismatch above 14%.[20-23] In order to minimize dislocation densities, many growth techniques such as Hydrid Vapor Phase Deposition (HVPE) or Metal Organic Chemical Vapor Deposition (MOCVD), start the growth process with a buffer layer grown at low temperature, and subsequently the growth temperature is increased.[24-26] The variation of temperature, although favorable for decreasing the dislocation density can induce strain heterogeneities often visible in the electron microscopy techniques.[27,28] In the present work, a tentative linearization method of the WH plots is presented and compared to conventional WH method for wurtzite aluminum gallium nitride and for orthorhombic molybdenum trioxide compounds, respectively. Although, to the best knowledge of the authors, it is the first time that analysis of size/strain plotting methods is applied directly to the latter, molybdenum trioxide has been used to study the mosaicity of mechanochemical reduction of powder MoO_3 by silicone to synthesize nanocrystalline $MoSi_2$ [29], nano-crystalline MoO_2[30] and hexagonal (h)-MoO_3 nanorods.[31] The method combines the analytical and graphical (WH) approaches by iteratively fitting of the measured curves with the objective of finding the best possible coefficients of the Pseudo-Voigts which linearize the graphical method. The linearization method, hereafter referred as LdCWH, acronym for Layer de-Convolution Williamson-Hall analysis, assumes that the total thickness of the crystal is divided into sections with specific mosaicity. In the dominant section, i.e., at the thicker slab, the coherence lengths, tilt angles and heterogeneous strains are calculated and assumed to be uniform within this layer. Furthermore, it is assumed that most of the diffraction curve is affected by the major slab and

the other contributions to the diffracted peak are due to the thinner slabs with different tilt angles, heterogeneous strains and coherence lengths. Not limited to single crystalline wurtzite nitrides or quasi-single crystalline orthorhombic molybdenum trioxide, as the case studies presented here, the proposed LdCWH method can be applied to any crystallographic lattice and to polycrystalline materials as well. In this work, WH plots using the integral breath and the full width at half maximum (FWHM), the former preferably used in the literature,[32-34] is also compared and discussed. The work presented here required the development of several software codes. Bond's method is used to derive a- and c- lattice parameters with high accuracy of the nitride crystal and the dedicated code, called Bond, also determined the FWHM of the ω-scans.[35-38] It applies the theoretical background described in ref. [39] and fits the experimental curves considering Pseudo-Voigt functions; Reciprocal Space Mapping, the RSM (for Reciprocal Space Mapping) code fits the experimental reciprocal space maps using 2D-Gaussians and is used here to confirm the lattice parameters derived via Bond's method; MROX, acronym for Multiple Reflection Optimization package of X-ray diffraction is first presented here and simulates and fits simultaneously 2θ-ω scans of multiple reflections. The earlier version of MROX, only targeted single reflections and with no name attributed was used in the work presented in refs.[35,40-44] Finally, the LdCWH method is the main subject of this manuscript whose software description is addressed to[45].

2. Samples and experimental technique description

Commercial aluminum gallium nitride (AlGaN) alloy is grown by MOCVD (Metal Organic Chemical Vapor Deposition) at NOVAGAN[46]. The AlGaN thickness is about 650 nm thick, measured by Rutherford Backscattering Spectrometry[47] and grown on top of a c − sapphire substrate. A thin AlN sacrificial layer, of less than 10 nm, was grown in-between in order to reduce the lattice mismatch between the substrate and the nitride compound. The AlGaN lattice parameters of a=3.167 Å and c=5.156 Å were derived using the extended Bond's method which is a high accuracy method for determining these fundamental quantities[39]. The method consists in measuring 4 (not shown) rocking curves (ω-scans), two symmetrical $0004^{+/-}$ and two asymmetrical $10\bar{1}4^{+/-}$. Although higher sensitivity reflections could be accomplished for higher Miller indexes such as $10\bar{1}5$ or even higher orders, the grazing incidence exit angle associated to this reflection obliges the scattering angle, 2θ-axis, to be at ~-105.9° which is not physically and geometrically implemented at the Bruker D8 AXS diffractometer used for *rocking* the sample. The $Al_{0.18}Ga_{0.82}N$ composition was derived using the AlN and GaN relaxed lattice parameters of $a_{AlN/GaN}$=3.111/3.1896 Å, $c_{AlN/GaN}$=4.980/5.1855 Å[48,49] as well as the relevant stiffness relevant coefficients of the same binaries $C_{13,AlN/GaN}$=99/103 GPa, $C_{33,AlN/GaN}$= 389/405 GPa.[50,51] These physical quantities were used as input in the Bragg law[52] and Poisson law[53] to consider biaxial strain. Lattice parameters and AlGaN composition uncertainties, derived from conventional propagation of error theory, are approximated to <0.001 Å and ~0.1%, respectively. At the primary X-ray beam side, a Cu source was used complemented with a Göbel mirror and a Ge $22\bar{4}0$ monochromator to reduce the horizontal divergence and to mitigate the Kα_2 radiation. The samples were measured using a double-axis diffractometer, where a slit of 0.1 mm was placed in front of the detector to accomplish the radial 2θ-ω scans and removed to probe the ω-scans. The diffracted intensity was collected using a point focus detector and recorded with appropriate software. The FWHM of the ω-scans below 0.13° for all measured reflections shows the very good crystalline quality of the AlGaN alloy.[54-56] Additional information about the crystalline quality of the AlGaN samples obtained via Rutherford backscattering/channelling and transmission electron microscopy can be found in ref .[42] The films show high single crystalline quality and the dominant defects are threading dislocations as typically found in III-nitride

heteroepitaxial films. Parallel and perpendicular to the sample surface lattice parameters were confirmed using reciprocal space mapping of an asymmetrical reflection, in this case $10\bar{1}5$, at the glancing incident angle geometry. Transformation between (Q_x,Q_z) reciprocal space units to lattice parameters for a hexagonal derived unit cell can be found, for example, in ref.[53]. Figure 1 shows the 2θ-ω scans of the 0002, 0004 and 0006 symmetrical reflections in the vicinity of the $Al_{0.18}Ga_{0.82}N$ Bragg peak. The diffractograms were simulated & fitted using the MROX code, which fits the three reflections simultaneously. The purpose of simultaneous fitting is not only to increase the lattice parameters accuracy, but utmost, it highlights the need to add $Al_{0.18}Ga_{0.82}N$ layers with different strain (or composition) and crystalline quality for the mosaicity analysis. MROX, first time published here, constitute the natural evolution of a code developed for the simulation of the 2θ-ω scans from single reflections of distorted crystals using the dynamical theory of X-ray diffraction. Several publications using previous version of this software can be found.[40-42] The simulation is accomplished using the recursive formalism described in ref.[57] based on the dynamical theory of X-ray diffraction. To take into consideration the crystalline quality, an attenuation factor, the static Debye-Waller factor, is added into the structure factor calculation.[58] The residual presence of $K\alpha_2$ radiation is taken into account and the instrumental function is executed through the convolution between the pure dynamical theory simulation and a Pseudo-Voigt function. The presence of a broad peak around 35.5 º is evident at 0002 diffractogram. This peak is attributed to a ~10 nm thin layer of strained AlN. The relaxed Bragg position should be centered at ~36º for a c_{AlN} lattice parameter of 4.980 Å.[48] The asymmetry of the main Bragg peak is clear, and increases as the scattering order increases – for 0006 the asymmetry is more pronounced than for 0004 and for 0004 higher than for 0002. The expected 2θ for a relaxed AlN for 0004 and 0006 reflections are ~76.4 º and ~136.3 º, respectively. These angular positions are out of the measurement range, thus, the expected diffracted broad AlN peak is absent in figures 1b) and c). Thickness, deformation (perpendicular to the sample surface, $\varepsilon_\perp$) and crystalline quality based on the static Debye-Waller (DW) factor for the individual $Al_{0.18}Ga_{0.82}N$ layers are schematically represented in figure 1d). According to the result of the 2θ-ω simulations, the resulting layered structure is, thereby, a set of three $Al_{0.18}Ga_{0.82}N$ layers all with the same composition but different strain (deformation) and crystalline qualities. The layer with the highest thickness is associated to the most intense centroid peak, whereas the other two layers are under compressive and tensile strains, respectively, but with much thinner thicknesses. Although the possibility of small extent of composition in-homogeneities cannot be discarded to explain the presence of the two lower intensity peaks, in the literature related to nitrides compounds, it is realized that phase separations are not common for the AlGaN crystal. Therefore, despite not being possible to separate with high certainty the effect of stoichiometry and strain due to the nature of the reflection measured (symmetric), heterogeneities in the AlGaN molar fraction can exist but with low probability, extension and magnitude.[59-63] Other factors that may affect the main Bragg peak asymmetry, include defects and instrumental or experimental constraints. However, the latter can be excluded in the present case, since the Göbel mirror and monochromator set of optics used for high-resolution measurements collimate the X-ray beam, minimizing its angular and wavelength divergences. Moreover, defects such as dislocations usually broaden the Bragg peaks symmetrically. The mosaicity to be determined corresponds to the thicker layer; nevertheless the same analysis is straightforward for the remaining layers.

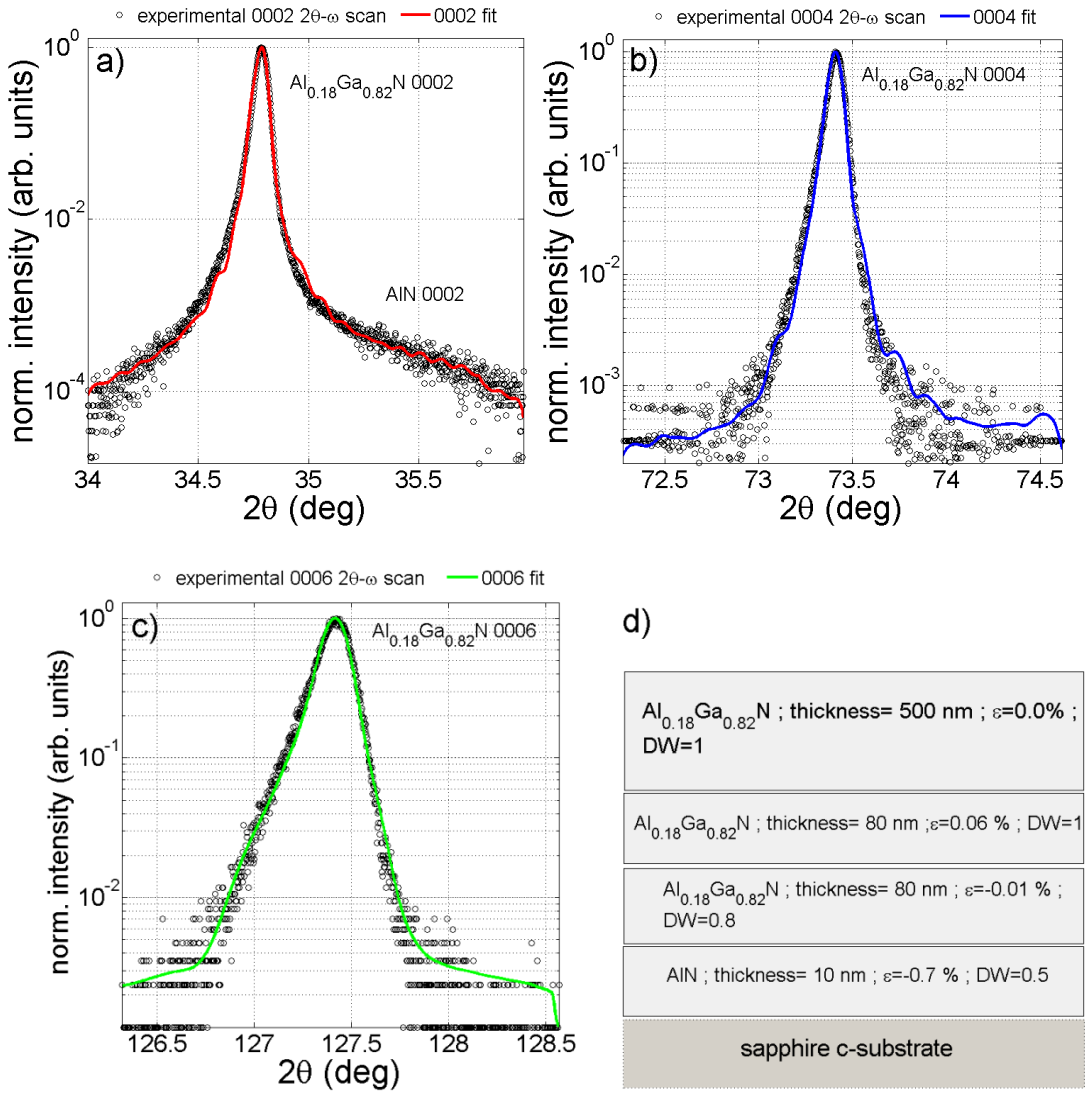

Figure 1 a-c) Experimental and simulation of the 2θ-ω scans around the vicinities of the $Al_{0.18}Ga_{0.82}N$ 0002, 0004, and 0006 Bragg peaks. The simultaneous simulations and fittings were accomplished using the MROX code[40-42]. d) Schematics of the top $Al_{0.18}Ga_{0.82}N$ surface layers with the corresponding layer thickness, deformation perpendicular to the sample surface ($\varepsilon_{\perp}$) and crystalline quality (DW).

α-molybdenum trioxide samples were grown by an evaporation-solidification method according to the procedure described in ref.[64]. The thickness of the as-grown crystals usually varies between 2 and 4μm, with typical lateral dimensions of about 2×5 mm^2.

3. Generic description of the Layer de-Convolution Williamson-Hall method

Theoretical background of conventional WH plots method as well as uncertainties calculation is described in the supporting information in section S1. Figure 2 shows a flowchart of the LdCWH algorithm for the example of the symmetric 00l reflections of AlGaN. LdCWH is accomplished in six steps and is exemplified using the ω-scans. In the first step, independent fits using three PVs for each ω-scan are performed. From the PVs coefficients derived in the independent fitting, a random PV generator combined with a genetic algorithm runs which

outputs the height (a_0), center (a_1), Gaussian width (a_2) and Lorentzian fraction (a_3). A convenient constant background is added to the sum of the three PVs of each reflection. Thus, a total of (4x3+1) x 3 independent variables, i. e., 13 variables per measured reflection are considered. The simultaneous fitting process, step II starts. For each combination of (a_1→center, a_2→Gaussian width, a_3→Lorentzian fraction belonging to the major slab, i. e., to the most intense peak from the accounted three PVs, a set of conventional WH method is plotted using y-axis → $\frac{\beta_\theta\,(FWHM)\times sin(\theta)}{\lambda}$, versus x-axis → $\frac{sin(\theta)}{\lambda}$.

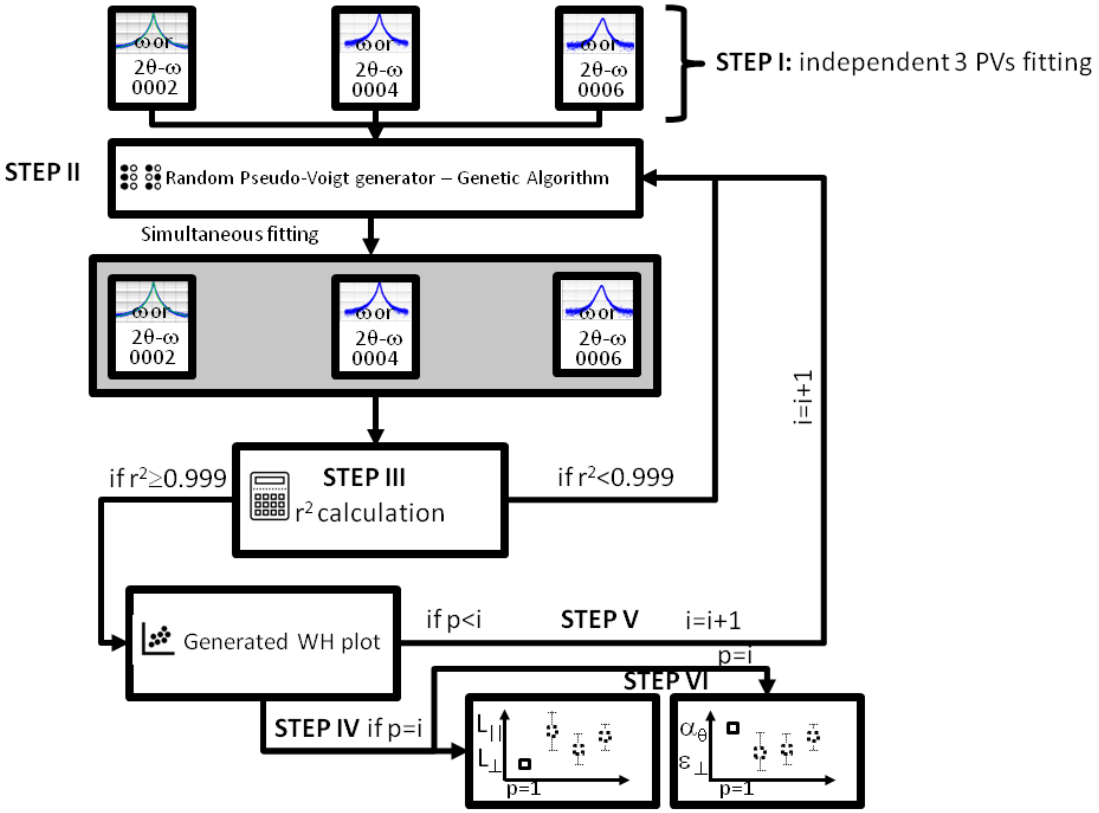

Figure 2 Flowchart of the Layer de-Convolution Williamson-Hall algorithm.

The selection of β_θ or the FWHM of the broadening is considered, accordingly, as the integral breadth or the full width at half maximum of the measured ω-scan. The linear correlation coefficient, r^2, is then calculated for each generated conventional WH plot. To accomplish the high linear correlation coefficient a combination of a Genetic[65] and Marquardt-Levenberg[66] algorithms is run: the Genetic Algorithm component, following a Monte-Carlo minimization strategy and corresponding to step II in figure 2, has the goal to find the best linear fit of the WH plot which provides the PV parameters output for fitting simultaneously the three PV of all reflections. This process is iteratively performed (step III) until the best solution for the PVs is found with reasonable linear fit of the WH plot (r^2≥0.999). Step III functionality corresponds, thus, to a decision - approval/rejection cycle of a given solution. The best solution corresponds to step IV in the flowchart (figure 2) and is a vector of (($L_{\|}$, α_θ),r^2) determined from the WH plot with magnitudes close to ($L_{\|}$, α_θ) derived from the analytical PV[67,68] and r^2>0.999. The calculated difference between the physical quantities derived via LdCWH and the analytical method in refs.[67,68] is defined in the code and several tests can be run until first best solution is found. To the best solution is indexed a p-number of iterations. p=1 corresponds to the first best solution found. Furthermore, the algorithm is run several p-number of times to consider a

reasonable number of best solutions and, thus, to attempt obtaining the upper and lower boundaries for the $L_{\|}$ and α_θ mosaicity physical quantities, respectively. The upper limit attributed to the p-number can be set on the LdCWH software. For each p-number is then calculated a pair of ($L_{\|}$, α_θ) and considered its cumulative standard deviation. The logic is that the $\sigma_{\text{p-number}=1}$ is null and $\sigma_{\text{p-number}=N}$ calls upon N number of iterations associated to

$$\sqrt{\frac{\sum_{i=1}^{p-number}\left|\left(L_{||},\alpha_\theta\right)_i-\langle L_{||},\alpha_\theta\rangle_{1\to i}\right|^2}{N}},$$

where $\left(L_{||},\alpha_\theta\right)_i$ is the calculated mosaicity pair for i=p-number and $\langle L_{||},\alpha_\theta\rangle_{1\to i}$is the average of the mosaicity pair from p-number=1 up to last p-number iteration. Finally, the uncertainty is interpreted as the delimiting standard deviation magnitudes (i=p-number). Explicitly, as the possible solutions for $L_{\|}$ and α_θ are determined, which depends on the allowed range attributed to the PV coefficients, $\sigma_{L_{\|}}$ and σ_{α_θ}will tend to continue increasing as per the random number generator obliges PV coefficients to be sufficiently different from each other. The increase at the standard deviations cannot continue in an endless loop because at some point $L_{\|}$ and α_θ will get closer to previous ones determined in previous p numbers, thereby decreasing the accumulated standard deviation by definition. # of p-numbers is provided by the user. The loop is represented in the flowchart as step V. In step VI, the evolution of the $\left(L_{||},\alpha_\theta\right)_{p-number}$ mosaicity pair for each p-number is plotted. Adaptation to 2θ-ω scans is straightforward.

4. Application of the LdCWH method

4.1 Aluminum gallium nitride ω-scans

Figures $3a_1$-a_2) to $3c_1$-c_2) show the experimental and simulated ω-scans using one PV and three PVs in the vicinities of the 0002, 0004 and 0006 $Al_{0.18}Ga_{0.82}N$ Bragg peaks. 0002, 0004 and 0006 are the allowed symmetrical reflections for the nitride compound studied. Only symmetric reflections are considered here because the tilt angle and coherence lengths (parallel and perpendicular to the substrate) are directly accessed. Asymmetric reflections are not considered since their shape will additionally depend on the twist.[68] Thereby, the analysis is limited to reflections whose planes are parallel to the sample surface. Assuming one PV function, the overall fit employing the Marquardt-Levenberg algorithm is not accurate as per the vicinities of the centroids are not well fitted (figures $3a_1$), $3b_1$) and $3c_1$)). In order to satisfy the ω-scans experimental data, especially for higher Miller indexes, the need of adding two layers with independent mosaicity, strain and/or composition is evident. As expected, aside adding two more PVs corresponding to the concatenated layers, the overall fit quality increases. The solution is shown in figures $3a_2$), $3b_2$) and $3c_2$). The partial PVs, PV1, PV2 and PV3 are also shown in the figures, where background is added to PV1+PV2+PV3. As observed in figures $3a_2$), $3b_2$) and $3c_2$), the calculated centers of the individual PVs are very close to each other which leads to high uncertainties of PV2 and PV3 centers (a_1), all PVs Gaussian widths (a_2) and Lorentzian fractions (a_3), respectively. Uncertainties calculation procedure is described in Supporting information 1 (S1). Inset figures $3a_1$-a_2) to $3c_1$-c_2) are shown the $L_{\|}$ and α_θ derived using Eqs. S.1a) and S.1b) reflecting the high uncertainties derived for the PV coefficients. The 1 PV and 3PVs coefficients, as well as $L_{\|}$ and α_θ and respective uncertainties are shown in table 1.

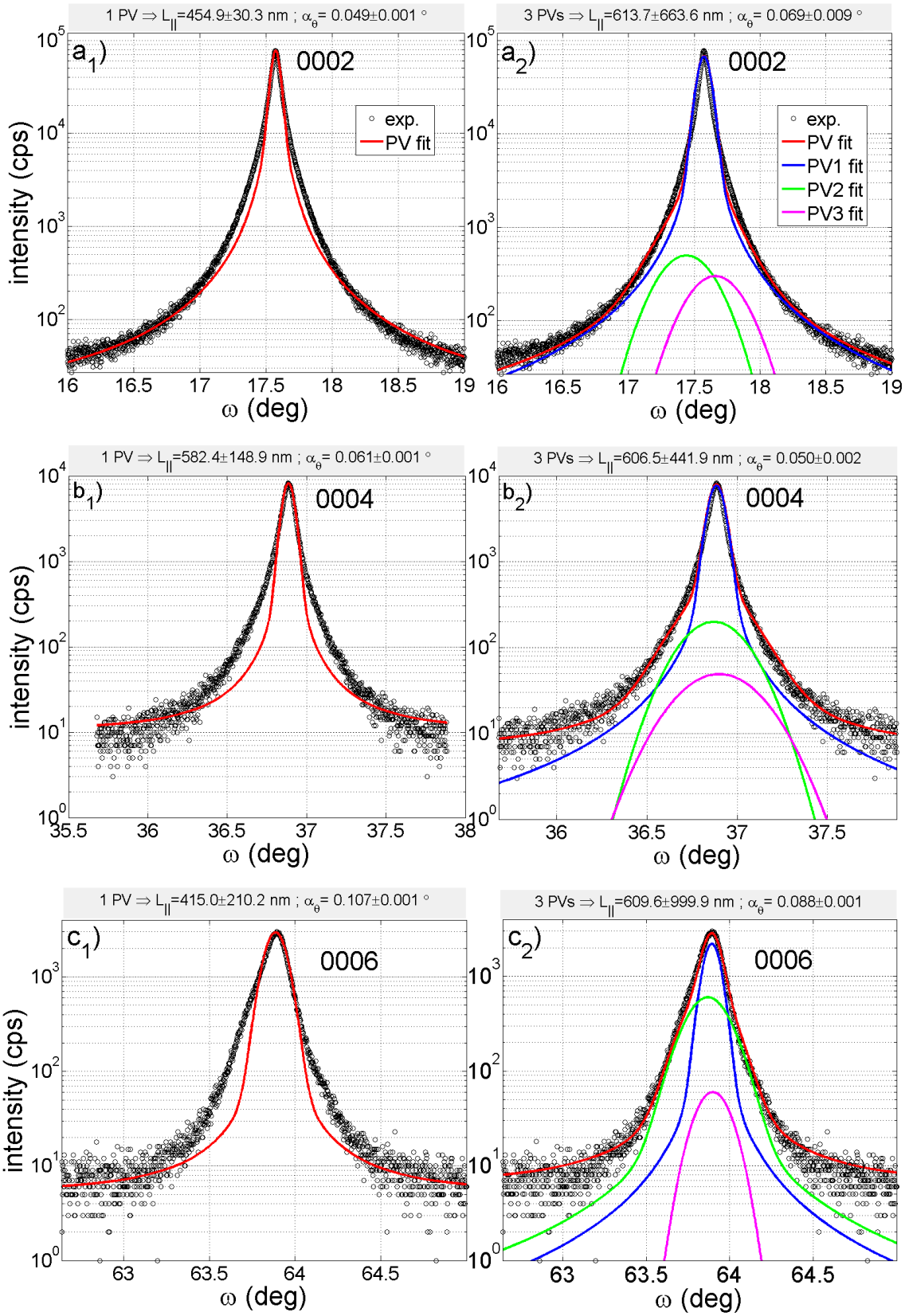
1 PV ⇒ L_II=454.9±30.3 nm ; α_θ= 0.049±0.001 °
a_1)
0002
exp.
PV fit
intensity (cps)
ω (deg)
3 PVs ⇒ L_II=613.7±663.6 nm ; α_θ= 0.069±0.009 °
a_2)
0002
exp.
PV fit
PV1 fit
PV2 fit
PV3 fit
ω (deg)
1 PV ⇒ L_II=582.4±148.9 nm ; α_θ= 0.061±0.001 °
b_1)
0004
intensity (cps)
ω (deg)
3 PVs ⇒ L_II=606.5±441.9 nm ; α_θ= 0.050±0.002
b_2)
0004
ω (deg)
1 PV ⇒ L_II=415.0±210.2 nm ; α_θ= 0.107±0.001 °
c_1)
0006
intensity (cps)
ω (deg)
3 PVs ⇒ L_II=609.6±999.9 nm ; α_θ= 0.088±0.001
c_2)
0006
ω (deg)

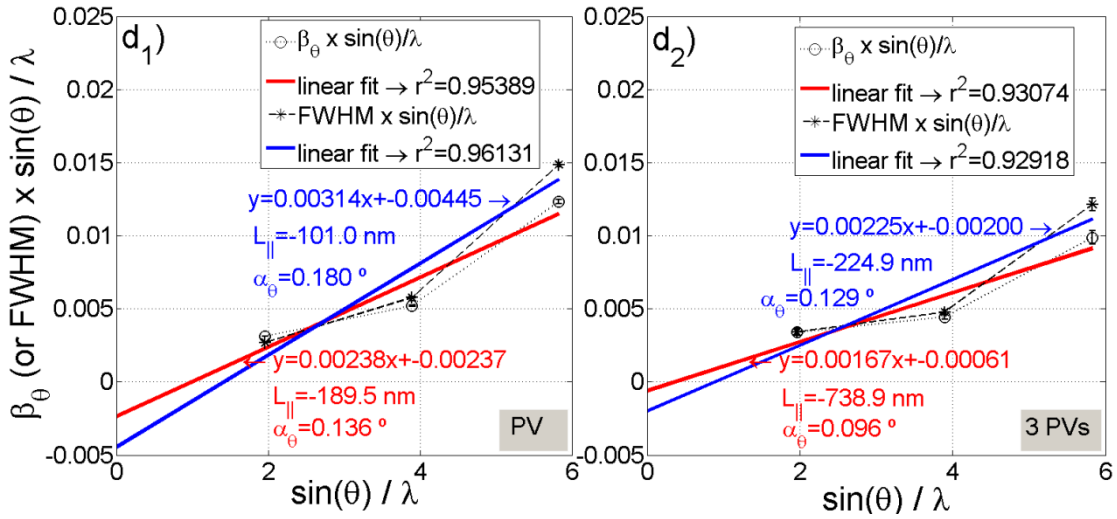

Figure 3 Experimental and simulated ω-scans around the $Al_{0.18}Ga_{0.82}N$ 0002, 0004 and 0006 Bragg peaks using one PV, (a_1, b_1, c_1), and three PVs (a_2, b_2, c_2). The output of the fitting used to build the WH plot is shown in d_1) for one PV and 3 PVs, d_2), respectively. The linear correlation coefficients (r^2) are ~0.954 and ~0.931 adopting the integral breadth and ~0.961 and ~0.929 applying the FWHM. All depicted linear correlation coefficients show a poor linear behavior of the integral breadth and FWHM as functions of the diffracted scattering vector.

Table 1 Lateral coherence length, $L_{||}$, tilt angle, α_θ, and respective uncertainties derived adopting one Pseudo-Voigt and three Pseudo-Voigts functions to simulate the ω-scans of all allowed symmetrical reflections of AlGaN. Pseudo-Voigts coefficients a_0, a_1, a_2, a_3 and respective uncertainties are also shown. * reflects the quantities derived via the integral breadths and ** the ones derived through the FWHM, respectively. $L_{||}$***, and α_θ *** were obtained using refs.[67-68].

ω-scan			a_0 (cps)	a_1 (deg)	a_2 (deg)	a_3 (adim.)	$L_{||}$ (nm) ***	α_θ (deg) ***
1 PV		0002	77405±50	17.5744±0.0003	0.0395±0.0004	0.50±0.03	455±30	0.049±0.001
		0004	8154±62	36.8854±0.0004	0.0424±0.0005	0.20±0.04	582±149	0.061±0.001
		0006	2946±86	63.8861±0.0007	0.0729±0.0008	0.11±0.05	415±210	0.107±0.001
3 PV	PV1	0002	69996±65	17.5742±0.0015	0.0499±0.0041	0.31±0.31	614±664	0.069±0.009
		0004	8202±156	36.8847±0.0004	0.0351±0.0009	0.23±0.15	607±442	0.050±0.002
		0006	2591±120	63.8925±0.0033	0.0596±0.0034	0.09±0.18	610±1000	0.088±0.001
	PV2	0002	1294±129	17.55±1.92	0.190±1.285	0.15±21.22	---	---
		0004	309±32	36.84±26.26	0.15±3.33	0.01±2.84	---	---
		0006	393±69	63.83±1.40	0.15±0.28	0.10±0.64	---	---
	PV3	0002	1495±125	17.59±0.91	0.14±1.69	0.02±30.07	---	---
		0004	220±42	36.92±45.60	0.15±5.79	0.01±4.84	---	---
		0006	192±34	63.95±3.19	0.15±0.68	0.1±1.44	---	---
WH			sin(θ)/λ	β_θ x sin(θ)/λ*	FWHM x	y=mx+y_0	$L_{||}$ (nm)	α_θ (deg)

			sin(θ)/λ [**]				
1 PV	0002	1.9600	0.0031199	0.0027029	0.00238x-0.00237 [*]	-189.5 [*]	0.136 [*]
	0004	3.8961	0.005217	0.0057683			
	0006	5.8285	0.012317	0.01485	0.00314x-0.00445 [**]	-101.0 [**]	0.180 [**]
3 PV	0002	1.9600	0.003400	0.003414	0.00167x-0.00061 [*]	-738.9 [*]	0.096 [*]
	0004	3.8961	0.004437	0.004774			
	0006	5.8285	0.009869	0.012130	0.00225x-0.00200 [**]	-224.9 [**]	0.129 [**]

From the linear fit, $y=mx+y_0$, the mosaicity quantities are found as:

$$L_{\parallel}=0.9/(2 \times y_0) \text{ and } \alpha_{\theta}=m.$$

Using one PV and three PVs, the mosaicity derived via conventional WH (figures 3d) results in $L_{\parallel,1PV}$=-189.5 nm / -101.0 nm and $\alpha_{\theta,1PV}$=0.136 ° / 0.180 ° and $L_{\parallel,3PV}$=-738.9 nm / -224.9 nm and $\alpha_{\theta,3PV}$=0.096 ° / 0.129 ° for both situations described (β_{θ} and FWHM), respectively (shown inset figure 3d) and table 1). Note that the fits employing 3 PVs do not consider the method described in Section 3 and flowchart of figure 2 and represent independent fits to the three diffraction curves. Comparing data from table 1, it is evident that analytical[67,68] and conventional Williamson-Hall methods do not agree. Then, using integral breadth and FWHM as ordinates of the Williamson-Hall plot (y_0), $L_{\parallel}$ is negative. $L_{\parallel}$ derived in this way, therefore, have no physical meaning differing considerably from the same quantities determined via analytical method using 3 PVs, ~610 nm, (table 1) and from what is usually found in the literature for nitrides.[69-74] Furthermore, conventional WH plot is not linear, r^2~0.954 using the integral breadth and one PV peak, whereas reaching 0.931 and 0.929 on three PVs by using the integral breadth and FWHM situations, respectively (Figures $3d_1$-d_2). $L_{\parallel}$ and α_{θ} quantities derived by applying one PV are not reliable. Although, using three independent PVs to fit the ω-scans increase the goodness of the fits, there are four major problems with this approach. First, a high linear correlation coefficient is not obtained. Second, the mosaicity parameters of $L_{\parallel}$ and α_{θ} are very different, if one considers the analytical or the conventional WH graphical methods; moreover, the WH provides negative coherence lengths which has no physical meaning. Finally, the uncertainties derived for the individual coefficients are too high due to the similarity of the three a_1 of individual PV (centers). Thereby, the individual fitting with 3 independent PVs of the ω-scans does not satisfy per se the requirement of having high linear fitting correlation coefficients. The lack of agreement between methods constitutes the motivation for the developed LdCWH analysis. By considering a layered structure, as the 2θ-ω simulations using the dynamical theory suggested (figure 1), the scattered intensity can be distributed in several different ways through the three PVs and several solutions are, thus, possible. The purpose of the LdCWH method is to find these solutions. In support information S2 a method is provided for accelerating the fitting convergence. Generically, the method searches the Lorentzian coefficients from the higher Miller indexes that match the mosaicity derived for the 0002. The best linear fit with a linear correlation coefficient of >0.999 is obtained as shown in figures $4a_1$-a_3) for randomly selected p-numbers of #5, #27 and #50. This figure shows the compressed LdCWH analysis considering the FWHMs and the integral breadths. The derived quantities $L_{\parallel}$ and α_{θ} inset figure 4a) agree with the ones found through the analytical method of refs. [67,68] depicted in table 1. Figures $4c_1$)-c_3) show the similarity between the fittings of all allowed ω-scans reflections from the p-numbers for the first 50 runs (p=5, p=27, p=50) represented in figure $4b_1$) for $L_{\parallel}$, figure $4b_2$-b_3) for α_{θ}, and in the flowchart as step VI, respectively.

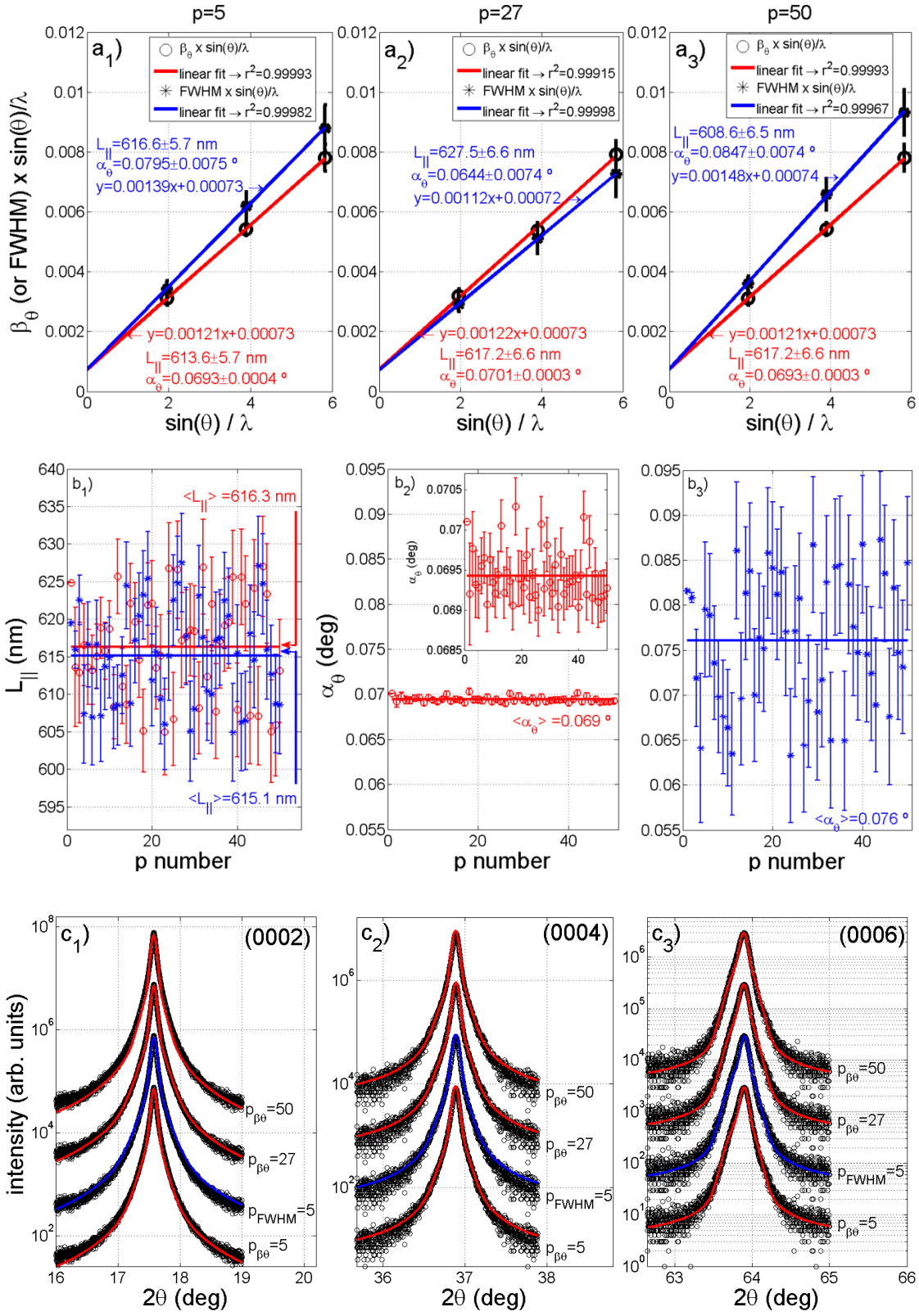

Figure 4 a_1-a_3) LdCWH method showing p-numbers of #5, #27 and #50 and considering the integral breadth and full width at half maximum broadenings plotted against the scattering vector length, $\sin(\theta)/\lambda$. The linear correlation coefficient, r^2, is above 0.999 for all p-numbers and for both broadening situations. Insets are given as the linear correlation fitting function together with derived $L_{||}$ and α_θ for the p-numbers indicated. b_1) Derived $L_{||}$ and uncertainty for all the 50 p-numbers accounted using the integral breadth (red) and the full width at half

maximum (blue). b_2) Derived α_θ and uncertainty for all the 50 p-numbers accounted using the integral breadth. The inset shows a zoom to highlight the uncertainties and to keep the same scale as in figure b_3) to highlight the higher uncertainties derived for the α_θ if one uses the full width at half maximum. c_1-c_3) Experimental and simulated ω-scans for all measured reflections for the p-numbers of #5, #27 and #50 considering the integral breadth. For comparison purposes the simulated curve for the p-number #5 is also plotted, but considering the broadening as the full width at half maximum.

While the absolute values for $L_\parallel$ and α_θ are the average of all calculated within the 50 p-numbers, 616.3 nm | 615.1 nm and 0.069 º | 0.076 º (using β_θ | FWHM), the range for the mosaicity parameters correspond to the last p-number as per standard deviation is calculated using all p-numbers in an accumulated fashion. The proposed range are then 616±7 nm and 0.069±0.001 º for $L_\parallel$ and α_θ, respectively. A higher tilt is found by applying the FWHM values, as concluded from comparison between figures $4b_2$) and $4b_3$). The feature is attributed to the increasing ratio for consecutive Miller indexes of the Lorentzian fractions

$$\frac{a_3(0002)}{a_3(0004)}\sim 1.35,\ \frac{a_3(0004)}{a_3(0006)}\sim 2.59,$$

and to the decrease of the same ratio for the Gaussian widths (half of FWHM),

$$\frac{a_2(0002)}{a_2(0004)}\sim 1.07,\ \frac{a_2(0004)}{a_2(0006)}\sim 0.91$$

using the PV coefficients from the p-number 50 as an example. These ratios imply a strong dependency of the broadening with the integral breadth. Thus, the use of FWHM as broadening may over estimate the tilt angle. In fact, as demonstrated in figure S.1, the tilt angle effect on the broadening is more pronounced on the width of the ω-scan, rather than on the shape of it. On the other hand, as the integral breadth increases as a function of the FWHM and the ratio between a_2 (or FWHM/2) for consecutive reflections is approximately equal to 1, then the y-axis for the WH plot increases more as the scattering vector increase, resulting in an increased slope, thus, higher tilt. To conclude this section, the straight line determined associated with the major crystal slab suggests in-homogenous mosaicity related to the $L_\parallel$ and α_θ present in the total $Al_{0.18}Ga_{0.82}N$ layer due to the different broadenings of the three PVs.

4.2 2θ-ω scans

In the case of the 2θ-ω scans, two case-studies are presented: $Al_{0.18}Ga_{0.82}N$ thick layer and the quasi-single crystalline α-MoO_3 bulk crystal. The latter is described as quasi-single crystal due to the fact that, although ω-scans are too broad not allowing to quantify $L_\parallel$ and the α_θ in a systematic form, $L_\perp$ and $\varepsilon_\perp$ show excellent properties (high $L_\perp$ and low $\epsilon_\perp$).

4.2.1 Aluminum gallium nitride 2θ-ω scans

Figures $5a_1$-a_2) to $5c_1$-c_2) show the experimental and simulated angular scans using one PV and three PVs 2θ-ω scans in the vicinity of the 0002, 0004 and 0006 $Al_{0.18}Ga_{0.82}N$ Bragg peaks. As in the case of the ω-scans, only reflections with planes parallel to the sample surface affect the vertical coherence length and the heterogeneous strain derived via the 2θ-ω.[68] Therefore, asymmetric reflections with a difference between the diffracted and incident wave vector non-orthogonal to the sample surface are excluded in the analysis limiting the number of reflections

to three. The increased difference between the fit using 1 PV and the 0002, 0004 and 0006 experimental data in figures $5a_1$, $5b_1$ and $5c_1$ is attributed to the increased resolution in the lattice parameter as the scattering order increases. Therefore, asymmetries become clearer for these reflections. Inset figures $5a_1$-a_2) provide the $L_\perp$ and $\varepsilon_\perp$. In Table 2 the relevant PV coefficients using one and three PVs, as well as derived $L_\perp$ and $\varepsilon_\perp$ calculated using the analytical method from ref.[67,68] and conventional WH are shown. As in the case of the ω-scans, the $L_\perp$ is found using y_0 ordinate as

$$L_\perp = 0.9/(2 \times y_0)$$

and the $\varepsilon_\perp$ is simply quantified as m/4 (m≡slope). As shown in the figures and in table 2, the $L_\perp$ determined from the analytical method using 1 PV is higher than the total $Al_{0.18}Ga_{0.82}N$ layer thickness of ~650 nm derived from the dynamical theory of X-ray diffraction and RBS. Additionally, by employing three PVs the same quantity is close to the expected value but the conventional WH analysis yields 129.3 nm and 669.5 nm by applying the integral breadth or the FWHM values, respectively (table 2). Although, the former amount could have a physical meaning and the linear correlation coefficient found for this situation is above 0.99 by employing the integral breadth, $L_\perp$ is far (129.3 nm) from the expected one of 650 nm and the standard WH analysis results in a low linear correlation coefficient of ~0.88 if analysis employs 1 PV (figure $5d_1$) or 3 PVs (figure $5d_2$). In both figures, the fitting of the experimental data using 1 and 3 PVs is executed without considering the method described in Section 2.

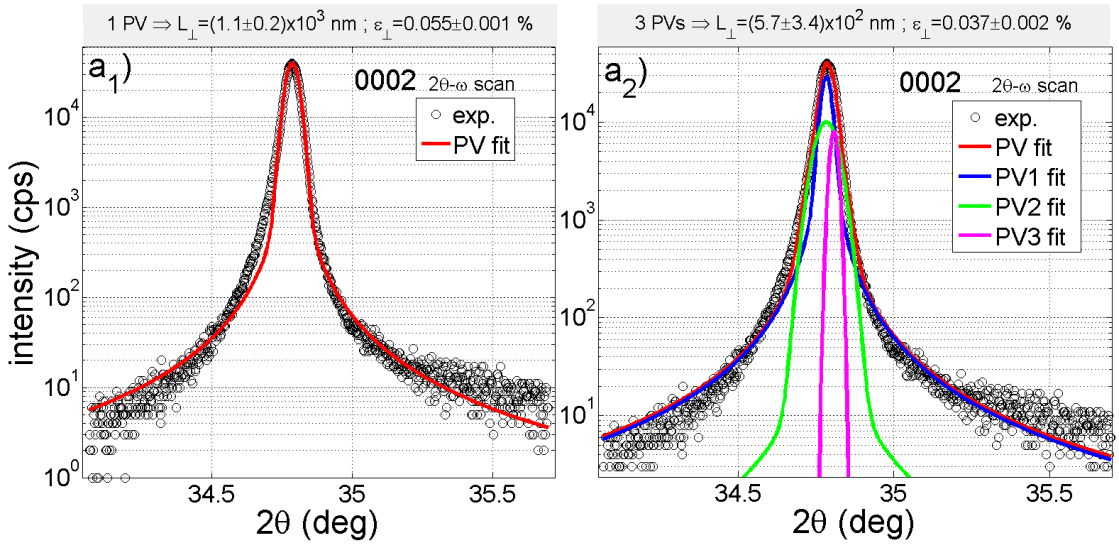

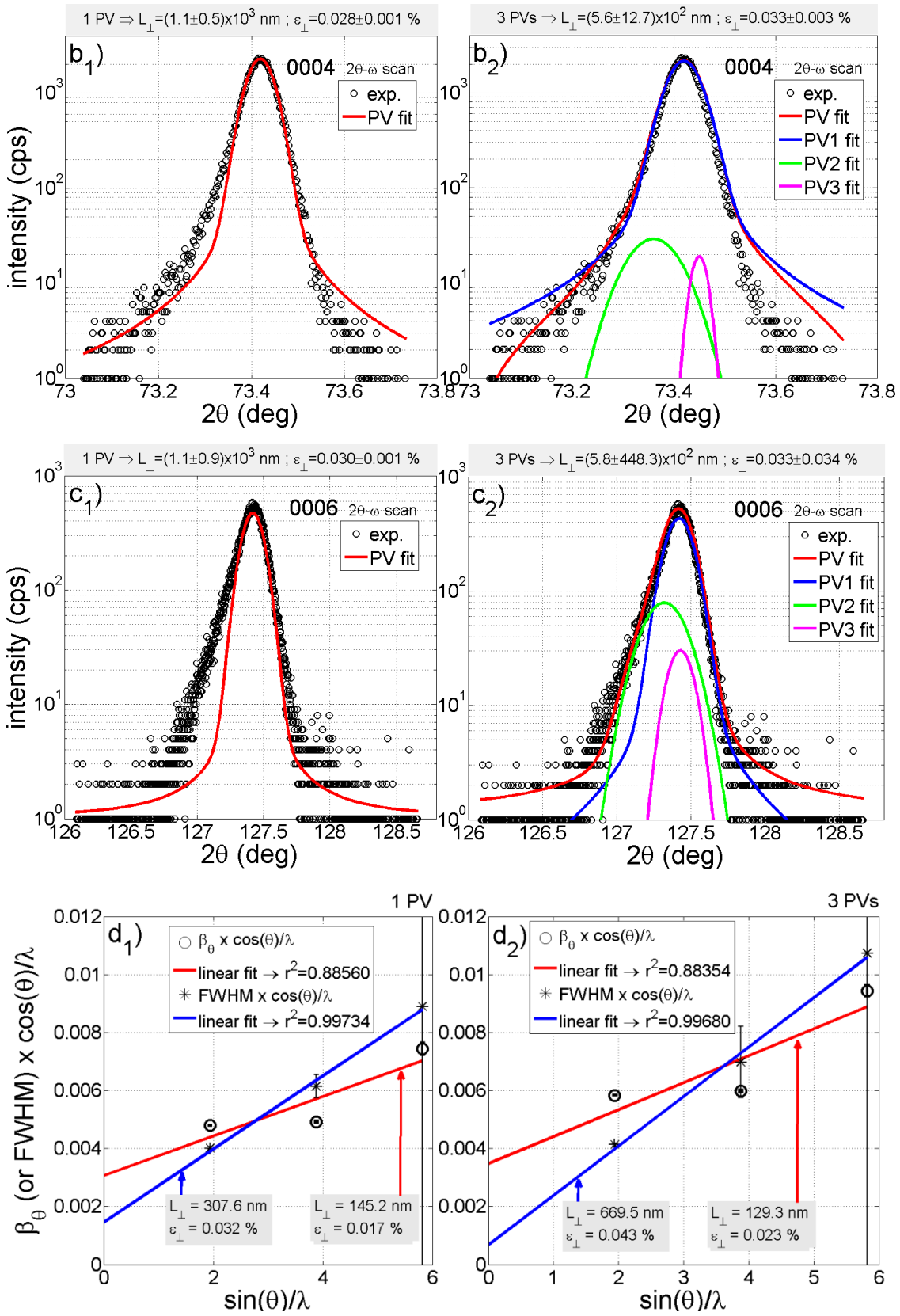

Figure 5 Experimental and simulated 2θ-ω scans around the $Al_{0.18}Ga_{0.82}N$ 0002, 0004 and 0006 Bragg peaks using one PV, (a_1, b_1, c_1), and three PVs (a_2, b_2, c_2). Derived $L_\perp$ and $\varepsilon_\perp$ via[67,68] is shown on top of each plot. The outputs of the fitting used to build the WH plot from the integral breadth and the FWHM are shown in d_1) and d_2), respectively. The linear correlation coefficients

(r^2) are ~0.886 and ~0.884 adopting the integral breadth and ~0.997 applying the FWHM for the conventional Williamson-Hall plotting and using 1PV and 3 PVs. The linear correlation coefficients show a poor linear behavior of the integral breadth and slightly less for FWHM as functions of the diffracted scattering vector.

Table 2 Perpendicular coherence length, $L_\perp$, heterogeneous strain, $\varepsilon_\perp$ and respective uncertainties derived adopting one Pseudo-Voigt and three Pseudo-Voigts functions to simulate the 2θ-ω scans of all allowed symmetrical reflections. Pseudo-Voigts coefficients a_0, a_1, a_2, a_3 and respective uncertainties are also shown. * symbolizes the quantities derived via the integral breadths and ** the ones derived through the FWHM, respectively. $L_\perp$***, and $\varepsilon_\perp$ *** were obtained using refs.[67,68].

2θ-ω-scan			**a_0 (cps)**	**a_1 (deg)**	**a_2 (deg)**	**a_3 (adim.)**	**$L_\perp$ (nm) *** **	**$\varepsilon_\perp$ (%) *** **
1 PV		0002	39777±34	34.7863±0.0001	0.0270±0.0001	0.10±0.01	1159±173	0.055±0.001
		0004	2285±23	73.4188±0.0003	0.0329±0.0003	0.10±0.05	1130±497	0.028±0.001
		0006	469±45	127.418±0.001	0.094±0.001	0.06±0.05	1147±881	0.030±0.001
3 PV	PV1	0002	28998±65	34.7829±0.0009	0.0191±0.0007	0.28±0.15	567±342	0.037±0.002
		0004	8202±156	36.8847±0.0004	0.0351±0.0009	0.23±0.15	564±1272	0.033±0.003
		0006	2591±120	63.8925±0.0033	0.0596±0.0034	0.09±0.18	579±44831	0.033±0.034
	PV2	0002	10000±856	34.7831±0.0016	0.041±0.002	0.01±0.13	---	---
		0004	32±7	73.36±1.87	0.06±1.04	0.05±20.81	---	---
		0006	78±13	127.32±0.49	0.169±0.173	0.0±1.9	---	---
	PV3	0002	8000±215	34.807±0.002	0.014±0.001	0.0±0.3	---	---
		0004	22±5	73.45±0.12	0.0181±0.3954	0.01±91.36	---	---
		0006	29±10	127.43±8.61	0.10±10.09	0.0±169.1	---	---
WH			**$\sin(\theta)/\lambda$**	**$\beta_\theta \times \cos(\theta)/\lambda$ *****	**FWHM x $\sin(\theta)/\lambda$ ******	**y=mx+y_0**	$L_\perp$ (nm)	$\varepsilon_\perp$ (%)
1 PV		0002	1.9600	0.0031199	0.0027029	0.00238x-0.00237 *	145.2 *	0.017 *
		0004	3.8961	0.005217	0.0057683			
		0006	5.8285	0.012317	0.01485	0.00314x-0.00445 **	307.6 **	0.032 **
3 PV		0002	1.9600	0.003400	0.003414	0.00167x-0.00061 *	129.3 *	0.023 *
		0004	3.8961	0.004437	0.004774			
		0006	5.8285	0.009869	0.012130	0.00225x-0.00200 **	669.5 **	0.043 **

Applying the LdCWH to the 2θ-ω scans, linear correlation coefficients of above 0.999 are found as shown in figures 6a_1-a_3). For comparison purposes, same p-numbers were chosen as in the case of the ω-scans but the solutions are valid for all p-numbers because, by definition, all of them satisfy the condition of having $r^2 \geq 0.999$. The deviation between the fit and the 0004

experimental data in figure 6a$_2$, especially for higher angles, is attributed to the simultaneous fitting condition of the three measured reflections while keeping valid the $r^2 \geq 0.999$ condition. In fact, the simultaneous fitting process forces, by definition, the mutual compensation between the fit of the three reflections in the minimization algorithm (goodness of the fit). The derived $L_\perp$ of ~511 nm is around the thickness of the surface AlGaN layer found using the dynamical theory of X-ray diffraction (500 nm) highlighting the coherence of the LdCWH method. By considering the boundaries determined through the LdCWH method, 511±10 nm, perfect agreement is found with the dynamical theory of X-ray diffraction simulations, as a static DW factor of unity was used in the simulations of figure 1 which reflects in a perfect crystal. Moreover, although not possible to discard the results obtained using the FWHM instead of the integral breadth, the boundaries found for the former are higher (figure 6b$_1$). $L_\perp$ of 541±27 nm found using the FWHM is 10% higher compared to the one derived using the dynamical theory of X-ray diffraction for the surface $Al_{0.18}Ga_{0.82}N$ layer. With respect to the derived $\varepsilon_\perp$, it is considerably higher (around 10% relative) for the situation of using the FWHM which implies that if this quantifier of the broadening is employed, then $\varepsilon_\perp$ and the $L_\perp$ will both be over estimated. To conclude this section there is a clear advantage of using the integral breadth as per the Lorentzian fraction constitutes around to 20-30% of the total broadening for the 0002, 0004 and less for the 0006 (around 1%). Furthermore, the LdCWH method enabled reconciling the analytical method with the conventional WH plot with linear correlation coefficients above 0.999.

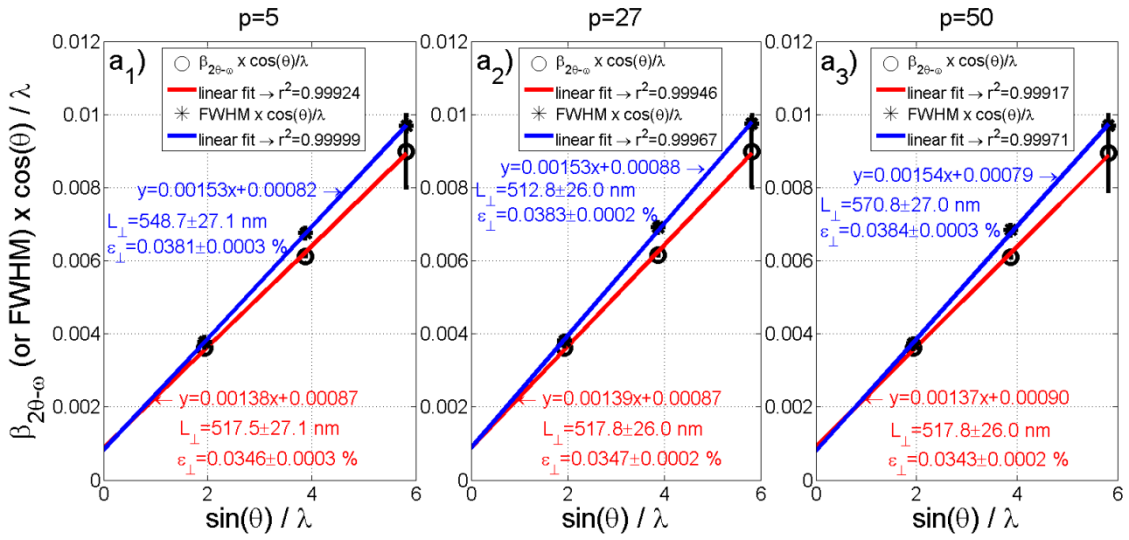

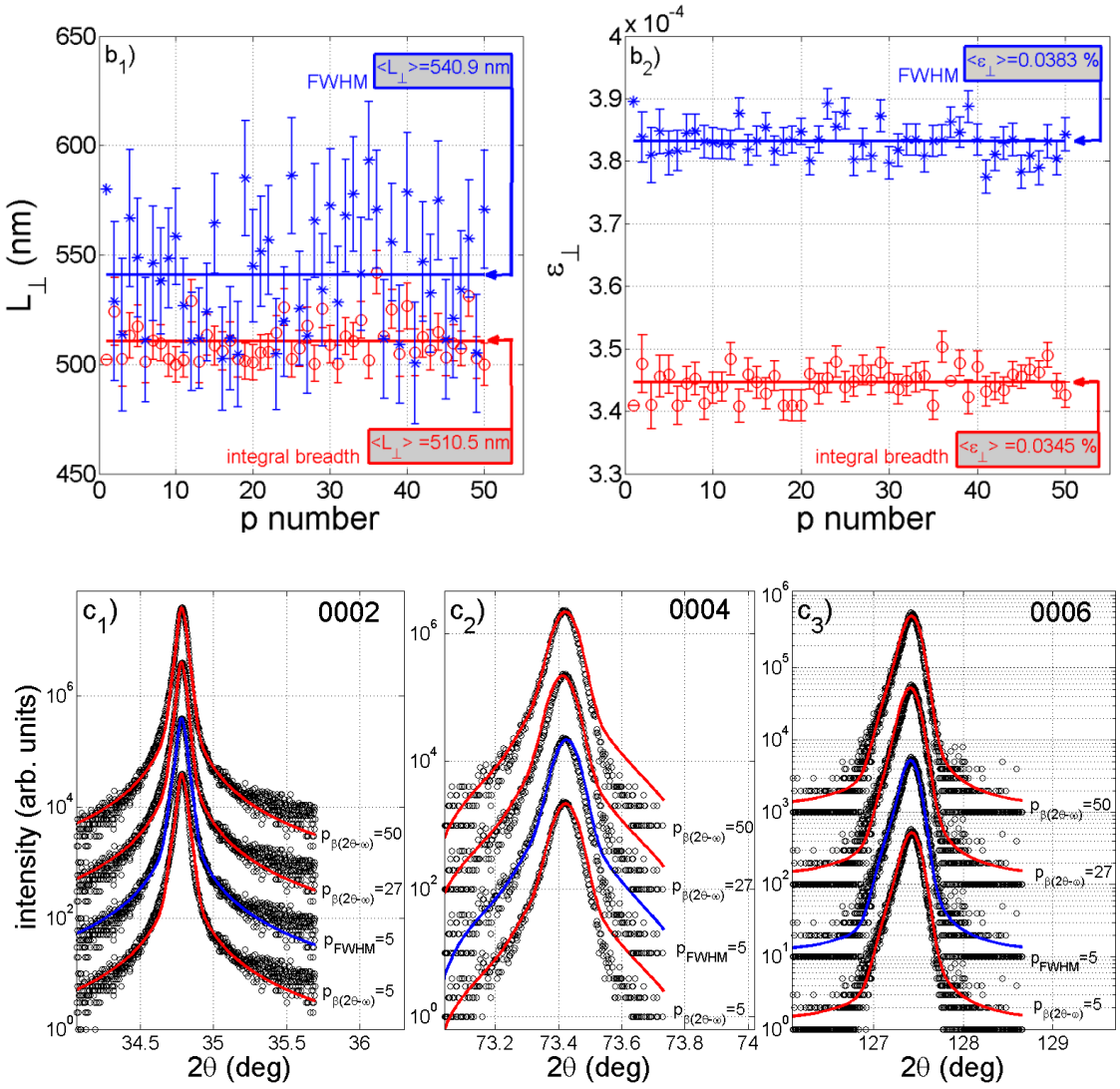

Figure 6 a_1-a_3) LdCWH method showing p-numbers of #5, #27 and #50 and considering the integral broadenings and full width at half maximum plotted against the scattering vector length, $\sin(\theta)/\lambda$. The linear correlation coefficient, r^2, is above 0.999 for all p-numbers and for both broadenings situations. The inset shows the linear correlation fitting function together with derived $L_\perp$ and $\varepsilon_\perp$ for the p-numbers indicated. b_1) Derived $L_\perp$ and uncertainty for all the 50 p-numbers accounted using the integral breadth and the full width at half maximum. b_2) Derived $\varepsilon_\perp$ and uncertainty for all the 50 p-numbers considered using the integral breadth. c_1-c_3) Experimental 2θ-ω scans and fits for all measured reflections for the p-numbers of #5, #27 and #50 considering the integral breadth and for comparison the simulated curve for the p-number #5 is also plotted but considering the broadening as the full width at half maximum.

4.2.2 Molybdenum trioxide 2θ-ω scans

Figures 7a_1-a_3) show the experimental and simulated 2θ-ω scans around $02\bar{2}0$, $04\bar{4}0$ and $06\bar{6}0$ α-MoO_3 Bragg peaks using 1 PV. Although, the asymmetry is considerably less than for the $Al_{0.18}Ga_{0.82}N$ compound, it tends to increase as the Miller indexes increase. The narrower 2θ-ω scans of the trioxide compared to the nitride is also related to a clear size effect as per in the case of the former a bulk crystal is used, whereas the latter is a thin film. Simulations using the

dynamical theory of X-ray diffraction (shown in section S3) also suggest slight asymmetry in the main Bragg peak indicating different regions in the crystal with slightly different deformations. Figure 7b) shows the conventional WH using the PV coefficients found in the fittings of figures 7a_1-a_3). The linear fit enables to obtain vertical coherence lengths of 154.4 nm (0.9/(2x0.00291)) and of 189.0 nm (0.9/(2x0.00238)) if the integral breadth and the FWHM are used as y-ordinates in the plots, respectively. These values are considered to be too low in view of the narrow 2θ-ω measured. With respect to the heterogeneous strain, values of 0.0163% (0.00065/4) and 0.0105 % (0.00042/4) are found by applying the integral breadth or the FWHM values, respectively. The linear correlation coefficients found for both situations, ~0.962 and ~0.964, also reveal the lack of proportionality between the broadening and the scattering vector length.

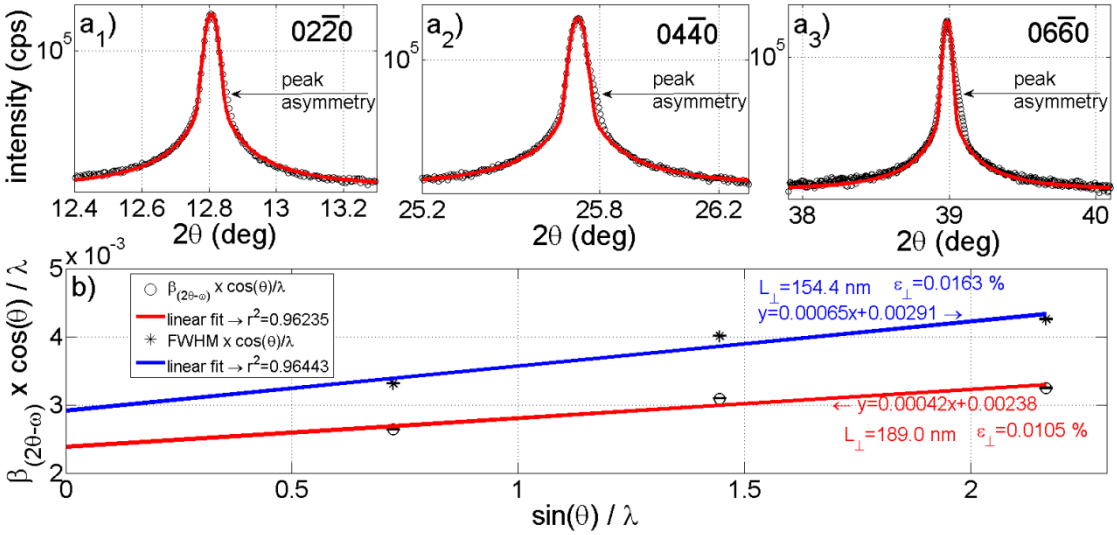

Figure 7 Experimental 2θ-ω scans and their fit around the 02$\bar{2}$0, 04$\bar{4}$0 and 06$\bar{6}$0 α-MoO_3 Bragg peaks using one PV, (a_1, a_2, a_3) and respective conventional WH plot, b). The linear correlation coefficient (r^2) is ~0.963 adopting the integral breadth and ~0.964 applying the FWHM for the conventional Williamson-Hall plotting. Both linear correlation coefficients show a poor linear behavior of the integral breadth and FWHM as functions of the scattering vector.

Applying the LdCWH, linearization of the conventional WH is accomplished as shown in figures 8a_1-a_3). High linear correlations coefficients are then found for all 50 p-numbers and three are selected as examples: p=3, p=22 and p=47. The evolution of the vertical coherence length ($L_\perp$) as well as the heterogeneous strain ($\varepsilon_\perp$) as functions of the p-number is shown in figures 8b_1-b_2). In figure 8b_2) a graphical inset is introduced to highlight the accumulated standard deviation in each p-number by using the integral breadth. The average $L_\perp$ and respective standard deviation is found to be 3883±56 nm and 3903±62 nm when using the integral breadth for the situation of the FWHM related broadening. With respect to $\varepsilon_\perp$ the averages and standard deviations found are 0.0557±0.0002 % and 0.0734±0.0006 % for the same related broadenings. As in the case of the nitride, $\varepsilon_\perp$ and its standard deviation derived using the FWHM are higher than the one derived via the integral breadth which is related to the Lorentzian character of the PV for all measured reflections (a_3<0.21) being reasonably far from a pure Gaussian profile. By not considering the shape related broadening, as is the case of the FWHM, $\varepsilon_\perp$ is overestimated.

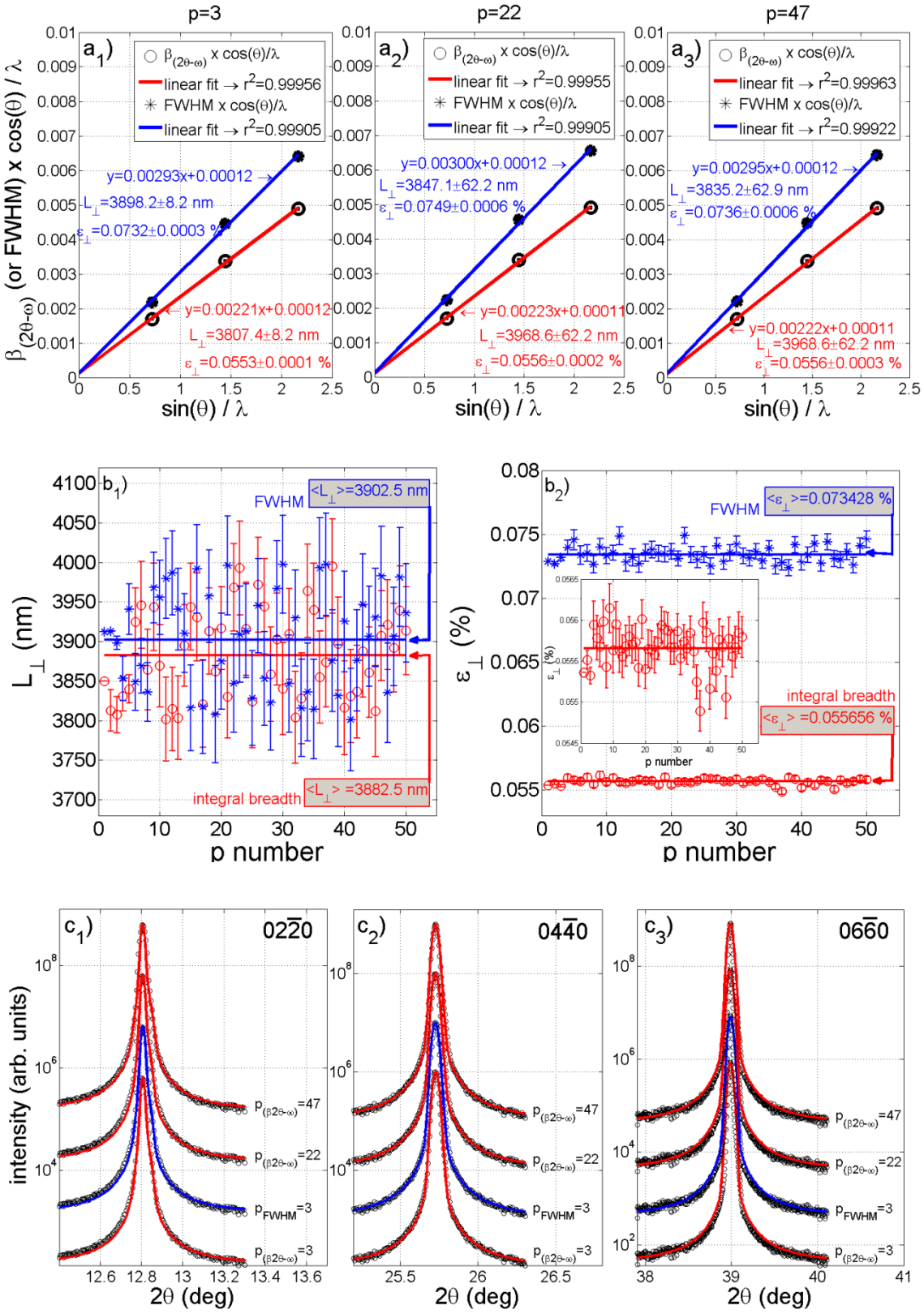

Figure 8 a_1-a_3) LdCWH method showing p-numbers of #3, #22 and #47 and considering integral breadth and the full width at half maximum broadenings plotted against the scattering vector length, $\sin(\theta)/\lambda$. The linear correlation coefficient, r^2, is above 0.999 for all p-numbers and for both broadening situations. The inset shows the linear correlation fitting function together with derived $L_\perp$ and $\varepsilon_\perp$ for the p-numbers indicated. b_1) Derived $L_\perp$ and uncertainty for all the 50 p-numbers accounted using the integral breadth and the full width at half maximum.

b_2) Derived $\varepsilon_\perp$ and uncertainty for all the 50 p-numbers accounted using the integral breadth. The inset shows a zoom to highlight the uncertainties and to focal point the higher uncertainties derived for the $\varepsilon_\perp$ if one uses the full width at half maximum instead of the integral breadth. c_1-c_3) Experimental and simulated 2θ-ω scans for all measured reflections for the p-numbers of #3, #22 and #47 considering the integral breadth and for comparison is also plotted the simulated curve for the p-number 3 but considering the broadening as the full width at half maximum.

5. Conclusions

A novel method for linearization of the conventional Williamson-Hall plots is developed and applied to a wurtzite aluminum gallium nitride thick (~600 nm) compound layer and to bulk α-molybdenum trioxide crystals. The Layer de-Convolution Williamson-Hall method, consists in an algorithm that searches the coefficients of three Pseudo Voigt functions which are used to simulate the ω- or 2θ-ω scans. The criterion of 3 PVs is based on the fact that, according to dynamical theory of X-ray diffraction simulations, the AlGaN layer can be divided into 3 slabs with specific thickness, deformation and static Debye-Waller factor, but same stoichiometry ($Al_{0.18}Ga_{0.82}N$). To the fitted PVs, conventional WH is plotted and the respective linear correlation coefficient (r^2) are calculated. It assumes the integral breadth or full width at half maximum to describe the curve broadening. A set of p-number solutions are found with $r^2 \geq 0.999$ (solutions having $r^2 < 0.999$ are rejected) and the absolute values of coherence lengths, tilt angle and heterogeneous strain normal to the substrate surface absolute quantities are determined as the averages of p-number fits. Boundaries are quantified as the last p-number as it constitutes the accumulated standard deviation calculated for all solutions given by each p-number. Applying the LdCWH method to the ω-scans of the AlGaN compound results in a lateral coherence length of ~600 nm and allows overcoming the negative lateral coherence length ambiguity which arises even if 3 PVs are used for the conventional WH plotting method. The derived tilt angle, <0.1º, agrees well with the ones found in the literature for the cases where pure symmetric peaks are measured for all allowed reflections. Moreover, LdCWH has the ability to closely match the lateral coherence length as well as the tilt angle derived via the analytical method. With respect to the 2θ-ω scans, the perpendicular coherence length is obviously limited to the crystal thickness. In the case of a conventional WH plot values between 145 nm to 307 nm were found using one PV and 129 to 670 nm for 3 PVs, respectively, whereas via LdCWH a value of 518 nm was found which is very close to the major $Al_{0.18}Ga_{0.82}N$ slab thickness derived via dynamical theory of X-ray diffraction. With respect to the heterogeneous strain of the $Al_{0.18}Ga_{0.82}N$ surface layer, it varies between 0.01% and 0.04% using the conventional WH and 1 PV and 3 PVs, respectively and a low variability oscillating around 0.034 % is found for all p-numbers using the LdCWH method. This small amount of heterogeneous strain agrees with the values found in the literature for GaN, AlN and related compounds. In the case of the molybdenum trioxide orthorhombic crystal, only 2θ-ω scans were measured because ω-scans were found to be quite broad, which should result in low lateral coherence lengths and high tilt angles. On the other hand, 2θ-ω scans are very sharp, surprisingly with full widths at half maxima even lower than for the nitride compound. The narrow 2θ-ω scans are reflected in the almost 4 μm of perpendicular coherence length (almost 10 times higher than for AlGaN). Heterogeneous strain perpendicular to the substrate surface is, in the case of the trioxide, slightly higher than for the AlGaN.

Funding information

This work was supported by the Fundação para a Ciência e a Tecnologia [grants PD/BD/143017/2018, PTDC/CTM-CTM/28011/2017, LISBOA-01-0145-FEDER-028011, CERN-FIS-PAR-0005-2017, UID/FIS/50010/2013, UID/Multi/04349/2013, UID/FIS/50010/2019, UID/FIS/00068/2019] as well as by projects PR87/19-22613 (Banco Santander-UCM) and MAT2016-81720-REDC (RED IMAGINE).

Conflicts of interest

There are no conflicts to declare.

References

[1] G. K. Williamson and W. H. Hall, Acta Metall., 1953, 1(1), 22-31.

[2] G. Singla, K. Singh and O. P. Pandey, Appl. Phys. A: Mater. Sci. Process., 2013, 113, 237-242.

[3] K. Venkateswarlu, A. Chandra Bose and N. Rameshbabu, Phys. B, 2010, 405 (20), 4256-4261.

[4] S. Brandstetter, P. M. Derlet, S. V. Petegem and H. V. Swygenhoven, Acta Mater., 2008, 56(2), 165-176.

[5] K. A. Aly, N. M. Khalil, Y. Algamal and Q. M. A. Saleem, Mater. Chem. Phys., 2017, 193, 182-188.

[6] V. D. Mote, Y. Purushotham and B. N. Dole, J. Theore. Appl. Phys., 2012, 6(6).

[7] N. S. Gonçalves, J. A. Carvalho, Z. M. Lima and J. M. Sasaki, Mater. Lett., 2012, 72, 36-38.

[8] P. Bindu and S. Thomas, J. Theore. Appl. Phys., 2014, 8, 123-134.

[9] P. Scardi, M. Ermrich, A. Fitch, E.-W. Huang, R. Jardin, R. Kuzel, A. Leineweber, A. Mendoza Cuevas, S. T. Misture, L. Rebuffi and C. Schimpf, J. Appl. Crystallogr., 2018, 51(3), 831-843.

[10] Heryanto, Hendri, B. Abdullah and D. Tahir, J. Phys.: Conf. Ser., 2017, 1080.

[11] T. Ungár and A. Borbély, Appl. Phys. Lett., 1996, 69, 3173.

[12] T. Ungár, J. Gubicza, G. Ribárik and A. Borbély, J. Appl. Crystallogr, 2001, 34, 298-310.

[13] T. Ungár, JCPDS-International Centre for Diffraction Data, 1997.

[14] D. Balzar and H. Ledbetter, J. Appl. Crystallogr., 1993, 26, 97-103.

[15] R. K. Nandi, H. K. Kuo, W. Schlosberg, G. Wissler, J. B. Cohen and B. Crist Jnr, J. Appl. Crystallogr., 1984, 17, 22-26.

[16] W. H. Schlosberg and J. B. Cohen, J. Appl. Crystallogr., 1983, 16, 304-308.

[17] T. Ungár, Scr. Mater., 2004, 51(8), 777-781.

[18] J. I. Langford, D. Louer and P. Scardi, J. Appl. Crystallogr., 2000, 33, 964-974.

[19] F. Sanchez-Bajo, A. L. Ortiz and F. L. Cumbrera, J. Appl. Crystallogr., 2006, 39(4), 598-600.

[20] V. S. Harutyunyan, A. P. Aivazyan, E. R. Weber, Y. Kim, Y. Park and S. G. Subramanya, J. Phys. D: Appl. Phys., 2001, 34, A35.

[21] M. Junaid, P. Sandstrom, J. Palisaitis, V. Darakchieva, C-L. Hsiao, P. O. A. Persson, L. Hultman and J. Birch, J. Phys. D: Appl. Phys., 2014, 47(14), 145301.

[22] H. J. Park, C. Park, S. Yeo, S. W. Kang, M. Mastro, O. Kryliouk and T. J. Anderson, Phys. Status Solidi C, 2005, 2(7), 2446-2449.

[23] C. Kisielowski, J. Kruger, S. Ruvimov, T. Suski, J. W. Ager, E. Jones, Z. Liliental-Weber, M. Rubin, E. R. Weber, M. D. Bremser and R. F. Davis, Phys. Rev. B, 1996, 54, 17745.

[24] X. Ni, Y. Fu, Y. T. Moon, N. Biyikli and H. Morkoç, J. Cryst. Growth, 2006, 290(1), 166-170.

[25] M. A. Mastro, O. M. Kryliouk, M. D. Reed, T. J. Anderson, A. Davydov and A. Shapiro, Phys. Status Solidi A, 2001, 188(1), 467-471.

[26] L. Zhang, J. Yu, X. Hao, Y. Wu, Y. Dai, Y. Shao, H. Zhang and Y. Tian, Sci. Rep., 2014, 4, 4179.

[27] Q.-J. Xu, B. Liu, S.-Y. Zhang, T. Tao, Z.-L. Xie, X.-Q. Xiu, D.-J. Chen, P. Chen, P. Han, R. Zhang and Y.-D. Zheng, Chin. Phys. B, 2017, 26(4), 047801.

[28] K. Jesbains, N. Kuwano, K. R. Jamaludin, H. Miyake, K. Hiramatsu, S. Suzuki, M. Mitsuhara, S. Hata and Y. Soejima, J. Mech. Eng. Sci., 2016, 10, 1908-1916.

[29] H. Ramezanalizadeh and S. Heshmati-Manesh, Adv. Mater. Res., 2011, 264-265, 1364-1369.

[30] M. Saghafi, A. Ataie and S. Heshmati-Manesh, Int. J. Mod. Phys.: Conf. Ser., 2012, 5, 441-447.

[31] S. K. Sen, T. C. Paul, S. Dutta, M. A. Matin, M. F. Islam and M. A. Hakim, Surf. Interfaces, 2019, 17, 100377.

[32] R. M. Chellab and K. H. Harbbi, AIP Conf. Proc., 2019, 2123, 020044.

[33] P. Pourghahramani and E. Forssberg, Int. J. Miner. Process., 2006, 79(2), 120-139.

[34] P. Scardi, M. Leoni and R. Delhez, J. Appl. Crystallogr., 2004, 37, 381-390.

[35] S. Magalhaes, N. Franco, I. M. Watson, R. W. Martin, K. P. O'Donnell, H. P. D. Schenk, F. Tang, T. C. Sadler, M. J. Kappers, R. A. Oliver, T. Monteiro, T. L. Martin, P. A. J. Bagot, M. P. Moody, E. Alves and K. Lorenz, J. Phys. D: Appl. Phys., 2017, 50(20), 205107.

[36] K. Lorenz, S. Magalhaes, N. Franco, N. P. Barradas, V. Darakchieva, E. Alves, S. Pereira, M. R. Correia, F. Munnik, R. W. Martin, K. P. O'Donnell and I. M. Watson, Phys. Status Solidi B, 2010, 247(7), 1740-1746.

[37] S. Magalhaes, M. Peres, V. Fellmann, B. Daudin, A. J. Neves, E. Alves, T. Monteiro and K. Lorenz, J. Appl. Phys., 2010, 108, 084306.

[38] M. Peres, S. Magalhaes, M. R. Soares, M. J. Soares, L. Rino, E. Alves, K. Lorenz, M. R. Correia, A. C. Lourenco and T. Monteiro, Phys. Status Solidi C, 2013, 10(4), 662-666.

[39] N. Herres, L. Kirste, H. Obloh, K. Kohler, J. Wagner and P. Koidl, Mater. Sci. Eng. B: Solid State Mater. Adv. Technol., 2002, 91-92, 425-432.

[40] S. Magalhaes, M. Fialho, M. Peres, K. Lorenz and E. Alves, J. Phys. D: Applied Physics, 2016, 49(13), 135308.

[41] P. Jozwik, S. Magalhaes, R. Ratajczak, C. Mieszczynski, M. Sequeira, A. Turos, R. Bottger, R. Heller, K. Lorenz and E. Alves, Phys. Status Solidi B, 2019, 256(5), 1800364.

[42] M. Fialho, S. Magalhaes, J. Rodrigues, M. P. Chauvat, P. Ruterana, T. Monteiro, K. Lorenz, E. Alves, Surf. Coat. Technol., 2018, 355, 29-39.

[43] J. S. Cabaço, MSc thesis, University of Porto, 2019.

[44] P. J. S. Mendes, MSc thesis, University of Lisbon, 2018.

[45] S. Magalhaes, J. S. Cabaço, J. P. Araujo and E. Alves, (2020), in preparation.

[46] Novagan, http://www.novagan.com/, (accessed on the 16th of June 2020).

[47] S. Magalhaes, I. M. Watson, S. M. Pereira, N. Franco, L. T. Tan, R. W. Martin, K. P. O'Donnell, E. Alves, J. P. Araujo, T. Monteiro and K. Lorenz, J. Phys. D: Appl. Phys., 2015, 48(1), 015103.

[48] M. Tanaka, S. Nakahata, K. Sogabe, H. Nakata and M. Tobioka, Jpn. J. Appl. Phys., 1997, 36(2).

[49] M. Yamaguchi, T. Yagi, T. Sota, T. Deguchi, K. Shimada and S. Nakamura, J. Appl. Phys., 1999, 85, 8502.

[50] W. Paszkowicz, R. Cerny and S. Krukowski, Powder Diffr., 2003, 18(2), 114-121.

[51] A. F. Wright, J. Appl. Phys., 1997, 82, 2833.

[52] L. Vegard, Z. Phys. Chem., 1921, 5(1), 17-26.

[53] C. Hammond, The Basics of Crystallography and Diffraction 4th edition, Oxford University Press, Oxford, 2015.

[54] M. A. Moram and M. E. Vickers, Rep. Prog. Phys., 2009, 72(3), 036502.

[55] M. A. Moram, M. E. Vickers, M. J. Kappers and C. J. Humphreys, J. Appl. Phys., 2008, 103, 093528.

[56] H. P. D. Schenk, E. Frayssinet, A. Bavard, D. Rondi, Y. Cordier and M. Kennard, J. Cryst. Growth, 2011, 314(1), 85-91.

[57] W. J. Bartels, J. Hornstra and D. J. W. Lobeek, Acta Cryst. A, 1986, A42, 539-545.

[58] N. Sousbie, L. Capello, J. Eymery, F. Rieutord and C. Lagahe, J. Appl. Phys., 2006, 99, 103509.

[59] O. Lagerstedt and B. Monemar, Phys. Rev. B, 1979, 19, 3064.

[60] I. Bryan, Z. Bryan, S. Mita, A. Rice, L. Hussey, C. Shelton, J. Tweedie, J.-P. Maria, R. Collazo and Z. Sitar, J. Cryst. Growth, 2016, 451, 65-71.

[61] A. Mogilatenko, V. Kuller, A. Knauer, J. Jeschke, U. Zeimer, M. Weyers, G. Trankle, J. Cryst. Growth, 2014, 402, 222-229.

[62] A. Pierret, C. Bougerol, S. Murcia-Mascaros, A. Cros, H. Renevier, B. Gayral and B. Daudin, Nanotechnology, 2013, 24(11), 115704.

[63] C. He, Q. Wu, X. Wang, Y. Zhang, L. Yang, N. Liu, Y. Zhao, Y. Lu and Z. Hu, ACS Nano, 2011, 5(2), 1291-1296.

[64] D. R. Pereira, M. Peres, L. C. Alves, J. G. Correia, C. Días-Guerra, A. G. Silva, E. Alves and K. Lorenz, Surf. Coat. Technol., 2018, 355, 50-54.

[65] D. E. Goldberg, Genetic Algorithms in Search, Optimization, and Machine Learning, Addison-Wesley, Massachusetts USA, 1989.

[66] J. J. More, The Levenberg-Marquardt algorithm: Implementation and theory, Numerical Analysis, Springer Berlin Heidelberg, Germany, 1978.

[67] Th. de Keijser, E. J. Mittemeijer and H. C. F. Rozendaal, J. Appl. Crystallogr., 1983, 16, 309-316.

[68] T. Metzger, R. Hopler, E. Born, O. Ambacher, M. Stutzmann, R. Stommer, M. Schuster, H. Gobel, S. Christiansen, M. Albrecht and H. P. Strunk, Philos. Mag. A, 1998, 77(4), 1013-1025.

[69] M. B. McLaurin, A. Hirai, E. Young, F. Wu and J. S. Speck, Jpn. J. Appl. Phys., 2008, 47, 5429.

[70] L. Jian-Qi, Q. Yong-Xin, W. Jian-Feng, X. Ke and Y. Hui, Chin. Phys. Lett., 2011, 28(1).

[71] R. Chierchia, T. Bottcher, S. Figge, M. Diesselberg, H. Heinke and D. Hommel, Phys. Status Solidi B, 2001, 228(2), 403-406.

[72] H.-M. Wang, J.-P. Zhang, C.-Q. Chen, Q. Fareed, J.-W. Yang and M. Asif Khan, Appl. Phys. Lett., 2002, 81, 604.

[73] H. Kang, S. Kandoor, S. Gupta, I. Ferguson, S. P. Guo and M. Pophristic, Phys. Status Solidi C, 2005, 2(7), 2145-2148.

[74] M. R. Laskar, T. Ganguli, N. Hatui, A. A. Rahman, M. R. Gokhale and A. Bhattacharya, J. Cryst. Growth, 2011, 315(1), 208-210.

[75] M. Birkholz, P. Fewster and C. Genzel, Mater. Charact., 2005